Biophysical Journal
Article

Biophysical Society

# Power Dissipation in the Cochlea Can Enhance Frequency Selectivity

Srdjan Prodanovic,[1] Sheryl M. Gracewski,[1,2] and Jong-Hoon Nam[1,2,*]
[1]Department of Mechanical Engineering and [2]Department of Biomedical Engineering, University of Rochester, Rochester, New York

ABSTRACT The cochlear cavity is filled with viscous fluids, and it is partitioned by a viscoelastic structure called the organ of Corti complex. Acoustic energy propagates toward the apex of the cochlea through vibrations of the organ of Corti complex. The dimensions of the vibrating structures range from a few hundred (e.g., the basilar membrane) to a few micrometers (e.g., the stereocilia bundle). Vibrations of microstructures in viscous fluid are subjected to energy dissipation. Because the viscous dissipation is considered to be detrimental to the function of hearing—sound amplification and frequency tuning—the cochlea uses cellular actuators to overcome the dissipation. Compared to extensive investigations on the cellular actuators, the dissipating mechanisms have not been given appropriate attention, and there is little consensus on damping models. For example, many theoretical studies use an inviscid fluid approximation and lump the viscous effect to viscous damping components. Others neglect viscous dissipation in the organ of Corti but consider fluid viscosity. We have developed a computational model of the cochlea that incorporates viscous fluid dynamics, organ of Corti microstructural mechanics, and electrophysiology of the outer hair cells. The model is validated by comparing with existing measurements, such as the viscoelastic response of the tectorial membrane, and the cochlear input impedance. Using the model, we investigated how dissipation components in the cochlea affect its function. We found that the majority of acoustic energy dissipation of the cochlea occurs within the organ of Corti complex, not in the scalar fluids. Our model suggests that an appropriate dissipation can enhance the tuning quality by reducing the spread of energy provided by the outer hair cells' somatic motility.

## INTRODUCTION

In the cochlea, acoustic energy is transmitted through the vibrations of the viscoelastic cochlear partition (1). Vibrating structures in the cochlea range from the 100- to 500-$\mu$m-wide basilar membrane to the 1- to 10-$\mu$m-tall stereocilia of the sensory receptor cells. Because of the micron scale, fluid dynamics in the cochlea is highly viscous (Reynolds number $<1$). A generally accepted premise is that viscous dissipation in the cochlear partition is detrimental to tuning and amplification of acoustic signals. To achieve physiological levels of tuning and amplification, the cochlear system is thought to need active mechanical feedback (2). The outer hair cells, one of two different types of sensory receptor cells in the mammalian cochlea, generate mechanical force to compensate for the dissipation (3).

Transmission of acoustic energy along the length of cochlear partition has been widely investigated. An isolated outer hair cell can generate electromotile forces on the order of $10^{-10}$ N (4,5). According to the measurement of cochlear input impedance (6–8), the acoustic power delivered through the stapes is on the order of $10^{-10}$ W at 40 dB sound pressure level. In theory, the outer hair cells can generate more power than the acoustic input power at 60 dB sound pressure level (9,10). On the other hand, how power is dissipated in the cochlea has been investigated at the cellular level (11–14), tissue level (15,16), and systems level (10).

Existing theories on how/where the power is dissipated in the cochlea are divergent. For example, most theoretical studies (17–25) use an inviscid fluid and lump the viscous effect into damping components, with damping properties adjusted to match the desired tuning quality and amplification factor. In contrast, a series of studies by Steele and his colleagues (26,27) explicitly incorporated the fluid viscosity while neglecting the dissipation within the organ of Corti. A recent study (28) developed a mouse cochlear model with viscous fluid and damping in the basilar membrane and the surrounding structure. Different assumptions for

*Submitted January 3, 2018, and accepted for publication February 22, 2019.*

*Correspondence: jong-hoon.nam@rochester.edu
Srdjan Prodanovic's present address is Department of Clinical and Experimental Medicine, Linköping University, Linköping, Sweden.

Editor: Mark Alber.
https://doi.org/10.1016/j.bpj.2019.02.022

dissipating mechanisms are partly responsible for the divergence in cochlear amplification theories.

We developed a computational model of cochlear mechanotransduction emphasizing the micromechanics of the organ of Corti (29–31). In an effort to better represent the dissipating mechanisms in the cochlea, fluid viscosity has been incorporated in this study, in addition to viscous dissipation within the organ of Corti structures. We investigated where and how the acoustic power is dissipated and how dissipating properties affect the frequency tuning quality of the cochlea. Because the model is linear, two asymptotic cases were simulated: when the outer hair cells' reactive force is most dominant (active) and when there are no active forces.

## METHODS

### Model overview

Similar to the earlier studies of Grosh and his colleagues (17,32), three physical systems are solved simultaneously (Fig. 1). They are the fluid dynamics in the cochlear ducts, the structural mechanics of the organ of Corti complex (OCC: the organ of Corti, tectorial membrane, and basilar membrane), and the electrophysiology of the outer hair cells. Two major changes were made to our previous model to investigate energy loss in further detail (30,31). First, fluid viscosity is explicitly considered in this study. Second, the nonstructural supporting cells (defined as the Hensen's, Claudius, and inner sulcus cells) were incorporated in an effort to represent their inertial and dissipating effect explicitly.

The fluid domain is separated by the OCC into two chambers (Fig. 1 *A*). The bottom chamber represents the scala tympani, and the top chamber represents the scala media and vestibuli. Note that most existing cochlear studies reduce the two fluid chambers into one, assuming that the differential pressure across the OCC is functionally relevant. However, several recent studies relaxed this simplification (18,33,34). Our model allows fluid in the top and bottom chambers to interact independently with the top and the bottom surfaces of the OCC, respectively. The entire domain is $H = 0.6$ mm tall and $L = 12.3$ mm long, including the 0.3 mm helicotrema. Model properties represent the gerbil cochlea.

The OCC mechanics is represented by a three-dimensional (3-D) finite element (FE) model (Fig. 1, *B* and *C*). Structural details of the OCC—such as the basilar and tectorial membranes, Dieters and pillar cells, the reticular lamina, and the outer hair cells—are incorporated (35). Those cells and tissues are represented with beam elements that can bend or stretch. The tectorial and basilar membranes are represented by a meshwork of beams consisting of radial and longitudinal components. Considering the strong anisotropy of the two membranes due to collagen fibers aligned in the radial direction ($y$ axis), the Young's modulus of the radial beams is greater than the Young's modulus of the longitudinal beams (Table 1). The basilar membrane is hinged along the spiral limbus and clamped along the spiral ligament. The edge of the tectorial membrane along the spiral limbus is clamped. The masses of the tectorial membrane and the basilar membrane were determined according to their anatomical dimensions (the *gray shaded area* in Fig. 1 *B*). The supporting cells are represented with isotropic tetrahedral elements, with mass density the same as water. A small elastic modulus is assigned to the supporting cells so that their contribution to stiffness is negligible (<5% of the total OCC stiffness). For all structural elements, the Poisson's ratio was given as 0.3.

The mechanotransduction and electromotility of the outer hair cells incorporated in this work are the same as in previous studies (30,36,37) and summarized in the Supporting Materials and Methods.

### Viscous fluid dynamics and fluid-structure interaction

The momentum and mass conservation equations are solved simultaneously (Eqs. 1, 2, and 3) for the entire fluid domain. After assuming a small-amplitude harmonic motion at radial frequency $\omega$, the two-dimensional (2-D) Navier-Stokes and continuity equations for an incompressible viscous fluid are

$$j\rho\omega u - \mu\nabla^2 u + \partial p/\partial x = 0, \tag{1}$$

$$j\rho\omega v - \mu\nabla^2 v + \partial p/\partial z = 0, \tag{2}$$

and

$$\partial u/\partial x + \partial v/\partial z = 0, \tag{3}$$

where $\nabla^2$ is the Laplace operator, $j$ is the imaginary unit, $p$ is the fluid pressure, $u$ and $v$ are the longitudinal ($x$) and transverse ($z$) velocity components,

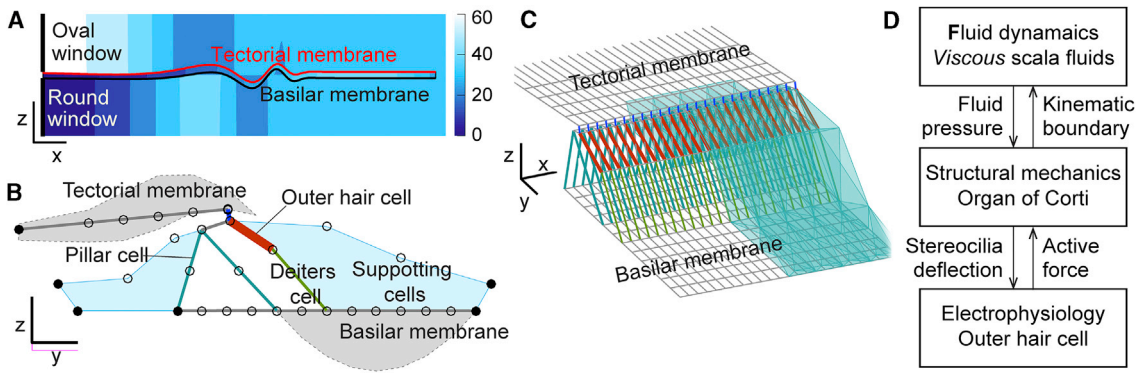


FIGURE 1 Cochlear model. (*A*) Fluid dynamics is shown. Cochlear scalae filled with viscous fluid are separated by the elastic OCC (here represented with the tectorial and basilar membranes). The color contour indicates fluid pressure when the oval window vibrates at 2 kHz with 1 $\mu$m/s amplitude. The scale bar represents 1 and 0.2 mm for the $x$ and $z$ axes. The color scale is in mPa. (*B*) OCC structures are shown. Circles indicates nodes. Filled circles are the nodes attached (fixed) to the spiral lamina/ligament. (*C*) A 3-D FE model is shown. The radial pattern of (*B*) repeats along the cochlear length to form the 3-D OCC structure. Shown is a 240-$\mu$m span of the model. All structural components are represented with beam elements, but supporting cells (in *light blue color*) were modeled with 3-D tetrahedral elements. (*D*) Schematics of how three physical problems are connected are given.

**TABLE 1 Model Parameters: Structure**

| Component | Parameters | $x = 2$ mm | $x = 10$ mm | Unit |
|---|---|---|---|---|
| Basilar membrane | width (arcuate, pectinate) | 53, 107 | 93, 187 | $\mu$m |
| | thickness (arcuate, pectinate) | 0.6, 3 | 0.14, 0.7 | $\mu$m |
| | YM (radial, longitudinal) | 1000, 0.4 | 1000, 0.1 | MPa |
| Outer hair cell | diameter, length | 9, 20 | 7, 50 | $\mu$m |
| | YM | 0.045 | 0.045 | MPa |
| Outer-hair-cell hair bundle | height, width | 2, 8 | 6, 8 | $\mu$m |
| | stiffness | 40 | 4.5 | mN/m |
| Pillar cell | diameter | 8 | 4 | $\mu$m |
| | YM | 50 | 50 | MPa |
| Deiters cell | diameter (body, phalange) | 10, 1.5 | 10, 0.8 | $\mu$m |
| | YM (body, phalange) | 5, 25 | 5, 25 | MPa |
| Reticular lamina | thickness, width | 2, 33 | 1, 57 | $\mu$m |
| | YM (radial, longitudinal) | 10, 0.2 | 2, 0.05 | MPa |
| Supporting cells | YM | 0.1 | 0.1 | kPa |
| Tectorial membrane | width (body, root) | 53, 27 | 140, 70 | $\mu$m |
| | thickness (body, root) | 30, 20 | 50, 25 | $\mu$m |
| | radial YM (body, root) | 1, 4 | 0.25, 1 | MPa |
| | longitudinal YM | 0.012 | 0.012 | MPa |
| Scala | endocochlear potential | 90 | 90 | mV |
| Outer-hair-cell stereocilia | maximal conductance | 90 | 27 | mV |
| | capacitance | 2.6 | 9 | nS |
| | resting open probability | 0.4 | 0.4 | |
| | maximal reactive force | 113 | 29 | pN |
| Outer-hair-cell membrane | equilibrium potential | 75 | 75 | mV |
| | resting potential | −53 | −37 | mV |
| | conductance | 230 | 39 | nS |
| | capacitance | 4.3 | 15 | pF |
| | electromechanical gain | 0.1 | 0.1 | nN/mV |

The values at different locations are obtained from these two sets of parameter values (at $x = x_1$ and $x_2$) using logarithmic interpolation. That is, $p(x) = p(x_1)\exp(a_L(x - x_1))$, $a_L = \log(p(x_2)/p(x_1))/(x_2 - x_1)$. Most geometrical parameters were obtained from Edge et al. (55). Other mechanical properties were justified in Nam and Fettiplace (35), with some adjustments in the tectorial membrane, and hair bundle properties. The electrical and mechanotransduction properties were from Nam and Fettiplace (36), which are based on measurements of Johnson et al. (80). YM, Young's modulus.

and $\mu$ and $\rho$ are dynamic viscosity and density of the fluid. The viscosity of water at 37°C, $\mu = 0.72$ mPa • s, was used in the simulations. The velocity of the oval window defines the input stimulation. At the round window, the fluid pressure is zero (pressure release boundary), and the longitudinal velocity gradient is zero. Because the 2-D fluid domain interacts with the 3-D structural domain, two longitudinal lines of the OCC represent the interacting surfaces: the lateral edge of the tectorial membrane and the center line of the basilar membrane. Those interacting lines (*surfaces*) were chosen because they are approximate midpoints of the radial span. Along the fluid-OCC interacting surfaces, the fluid velocity is determined by the velocity of the interacting OCC structures or

$$u = 0 \tag{4}$$

and

$$v = a_{32}\beta(j\omega\pi z_{IS}), \tag{5}$$

where $z_{IS}$ is the z-displacement at the interacting surface of the OCC. The parameter $\beta$ is the ratio between the basilar membrane width and the cochlear chambers' width. The parameter $a_{32}$ accounts for 3-D to 2-D conversion, assuming a half-sine radial velocity profile for the interacting surface. The conversion satisfies conservation of energy on the fluid-structure interface.

The fluid force acting on the OCC along the interacting lines is

$$f_{fluid} = a_{23}A_{IS}p, \tag{6}$$

where $A_{IS}$ is the surface area of the OCC at the location of contact with the fluid. The parameter $a_{23}$ converts the pressure of the 2-D fluid domain into nodal forces acting on the 3-D structural domain.

No-slip boundary conditions are applied along all fluid-structure boundaries. This no-slip boundary condition creates a velocity gradient, which is responsible for the energy dissipation in the viscous fluid (Fig. 2). Most energy dissipation in the extra-OCC fluids occurs in the viscous boundary layer. For frequencies from 0.1 to 30 kHz, the boundary layer thickness ranges from 300 to 15 $\mu$m. To resolve fluid motion in the boundary layer with reasonable computational time, a nonuniform grid (Fig. 2 *A*) was used to solve the fluid dynamics equations (Eqs. 1, 2, and 3).

## Electrophysiology of the outer hair cell

The mechanoelectrical transduction theory from previous studies (38,39) was used to obtain the relationship between the normalized transduction current ($p_o$) and hair bundle displacement ($x_{HB}$). According to the gating compliance theory (40), the action of transduction channels results in a force ($f_{MET}$) proportional to the transduction current or

$$f_{MET} = g_{MET}\delta p_o(x_{HB}, \omega), \tag{7}$$

where $g_{MET}$ is the maximal gating force. The constant $g_{MET}$ ranges from 100 pN at the cochlear base to 10 pN at the apex (38). The $f_{MET}$ is applied as a pair of equal and opposite forces at the tip and base of the hair bundle so that it deflects the bundle. The outer hair cell's somatic force, $f_{OHC}$, is proportional to the change of the transmembrane voltage, $V_m$,

$$f_{OHC} = g_{OHC}\delta V_m(p_o, \omega), \tag{8}$$

where $g_{OHC}$ is a constant representing the outer hair cell's electromechanical gain. A constant value of $g_{OHC} = 0.1$ nN/mV (5) was used independent

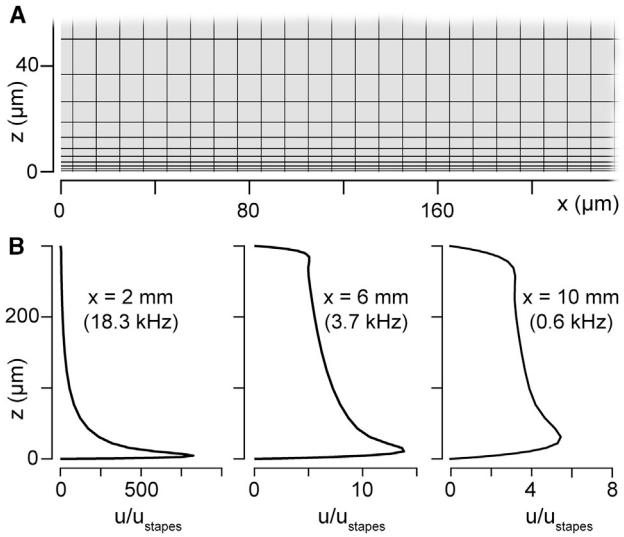


FIGURE 2 Fluid velocity profile and viscous boundary layer. The fluid velocity in the $x$ direction ($u$) varies with distance from the fluid-structure interacting surface. The velocity gradient ($\partial u/\partial z$) is responsible for viscous dissipation. (*A*) A nonuniform mesh grid is shown. To resolve the steep velocity gradient along the vertical ($z$) axis, a finer grid size (0.6 $\mu$m) was used at the fluid-structure boundary ($z = 0$). To save computation cost, the vertical grid size was increased up to 20 $\mu$m. The longitudinal grid size was fixed at 10 $\mu$m. (*B*) Velocity profiles versus distance from the fluid-structure interface at three different frequencies are shown. At the fluid-structure interface (at $z = 0$ and 300 $\mu$m), the fluid velocity is zero because of the nonslip condition.

of the location. The outer hair cell's somatic force $f_{OHC}$ was applied along the axis of the outer hair cell as a pair of equal and opposite forces at the extremities of the cell body so that depolarization (increasing $V_m$) contracts the cell. In this work, the term "active" or "passive" refers to the state with or without outer hair cell's active feedback, i.e., $g_{MET} = g_{OHC} = 0$ when passive.

The relationships between $x_{HB}$, $p_o$, and $V_m$ and the related model properties are presented in Eqs. A11 and A19; Fig. S4.

## Numerical implementation

For small harmonic excitation at radial frequency $\omega$, the discretized equation of motion of the OCC can be written in terms of stiffness, mass, and damping matrices **K**, **M**, and **C** as

$$\left(\mathbf{K} - \omega^2\mathbf{M} + j\omega\ \mathbf{C}\right)\mathbf{x} = \mathbf{f}_{fluid} + \mathbf{f}_{OHC} + \mathbf{f}_{MET}, \qquad (9)$$

where **x** is the column vector of nodal displacements and $\mathbf{f}_{fluid}$, $\mathbf{f}_{OHC}$, and $\mathbf{f}_{MET}$ are force vectors because of fluid pressure, outer hair cell's somatic force, and stereociliary bundle active force, respectively.

Viscous fluid mechanics, structural mechanics, and outer-hair-cell electrophysiology were solved simultaneously in the frequency domain. Unknown variable vectors are the fluid pressure **p**, fluid longitudinal and transverse velocities **u** and **v**, OCC nodal displacement **x**, and the vector **e**, which contains the electrophysiological variables ($p_o$ and $V_m$ of the outer hair cells).

The governing equations (Eqs. 1, 2, 3, and 9), fluid-structure interaction relationship (Eqs. 4 and 5), and all the forces (Eqs. 6, 7, and 8) can be written in combined matrix form as

$$\begin{bmatrix} \mathbf{A}_{f11} & 0 & \mathbf{A}_{f13} & 0 & 0 \\ 0 & \mathbf{A}_{f22} & \mathbf{A}_{f23} & \mathbf{A}_{fx1} & 0 \\ \mathbf{A}_{f31} & \mathbf{A}_{f32} & 0 & \mathbf{A}_{fx2} & 0 \\ 0 & 0 & \mathbf{A}_{xf} & \mathbf{A}_{xx} & \mathbf{A}_{xe} \\ 0 & 0 & 0 & \mathbf{A}_{ex} & \mathbf{A}_{ee} \end{bmatrix} \begin{bmatrix} \mathbf{u} \\ \mathbf{v} \\ \mathbf{p} \\ \mathbf{x} \\ \mathbf{e} \end{bmatrix} = \begin{bmatrix} \mathbf{b}_1 \\ 0 \\ \mathbf{b}_2 \\ 0 \\ 0 \end{bmatrix}. \qquad (10)$$

Submatrices on the left-hand side of the Eq. 10 are discretized forms of the governing equations. $\mathbf{A}_{f11}$ and $\mathbf{A}_{f22}$ represent the first two terms in the Navier-Stokes equations (Eqs. 1 and 2, respectively). $\mathbf{A}_{f13}$ and $\mathbf{A}_{f23}$ represent the third term (the pressure gradient term) in Eqs. 1 and 2, respectively. $\mathbf{A}_{fx1}$ represents the Navier-Stokes equation boundary condition along the OCC-fluid interacting surfaces, Eq. 5. $\mathbf{A}_{f31}$ and $\mathbf{A}_{f31}$ represent the first and second terms, respectively, of the continuity equation, Eq. 3. $\mathbf{A}_{fx2}$ represents the fluid-structure interaction of Eq. 5. $\mathbf{A}_{xf}$ represents the force boundary condition of the OCC due to fluid pressure, Eq. 6. $\mathbf{A}_{xx}$ represents the OCC mechanics equation, Eq. 9. $\mathbf{A}_{xe}$ defines the outer-hair-cell forces acting on the OCC according to Eqs. 7 and 8. $\mathbf{A}_{ex}$ and $\mathbf{A}_{ee}$ represent the relationship between the outer hair cells' stereociliary bundle displacements and mechanotransduction currents. The right-hand side of Eq. 10 is the vector representing the oval and round window boundary conditions: $\mathbf{b}_1$ for the Navier-Stokes equation, $\mathbf{b}_2$ for the continuity equation.

The program is written in MATLAB (The MathWorks, Natick, MA). No specific toolbox was used. The assembled system has ~220,000 degrees of freedom. In a personal computer (Intel i7-6700 processor, 16 gigabytes memory), it takes ~10 s to solve for one frequency. The majority of time is spent on updating frequency-dependent components of the submatrices in Eq. 10. The code is available upon request.

## Dissipation in the OCC

In addition to the dissipation in the extra-OCC (scala) fluids, the acoustic energy is dissipated within the OCC. Intra-OCC dissipation results from different components: 1) damping from acellular structures (the tectorial and the basilar membranes); 2) damping from the organ of Corti cells including the outer hair cells, the Deiters cells, and the supporting cells; and 3) damping from the extracellular fluid within the organ of Corti (e.g., fluids in the subtectorial space). The damping matrix **C** in Eq. 9 represents damping from all intra-OCC sources.

The Rayleigh damping was used to approximate the damping of the beam elements of the OCC, where the damping matrix is formed using the stiffness and the mass matrices

$$\mathbf{C} = \alpha_C\mathbf{K} + \beta_C\mathbf{M}. \qquad (11)$$

We let $\alpha_C = 0$ ms and $\beta_C = 20$ ms$^{-1}$. Similar to other studies, these values of damping parameters were chosen to obtain physiological level of amplification and tuning. Later in Results, our chosen value of $\beta_C$ is justified by comparing viscoelastic responses of our FE model with experimental measurements.

It is a general practice to use Rayleigh damping in the FE analysis to build the damping matrix by copying the matrix form (connectivity) from the stiffness and the mass matrix. If an element connects two nodes in matrices **M** and **K**, the connectivity between those two nodes is represented by nonzero values in relevant off-diagonal terms. Using the **M** and/or **K** matrices to form **C** matrix ensures that the **C** matrix also has reasonable connectivity. The level of damping is solely represented by the coefficient $\alpha_C$ and $\beta_C$. Note that Rayleigh damping is "viscous damping" in that the damping force is proportional to velocity. The root cause of intra-OCC dissipation must be the viscous fluid losses within and around the OCC structures. Our Rayleigh damping is one way to represent those viscous losses.

Alternative forms of damping were used for three model components: the subtectorial space, the outer hair cells, and the nonstructural supporting

cells. The subtectorial space damping $c_{STS}$ is derived assuming Couette flow between two plates as in (41),

$$c_{STS} = \mu A_{STS}/h_{HB}, \tag{12}$$

where $A_{STS}$ is the surface area of the subtectorial space defined by the product of the reticular lamina width ($b_{RL}$) and the longitudinal span between hair cells ($\Delta x$). $h_{HB}$ is the hair bundle height.

Because the outer hair cells are the actuators and their damping cancels the active force directly, their damping properties may be important. Therefore, to be explicit, the outer hair cells' dissipating property was defined independently. The axial damping coefficient of an outer hair cell was estimated to be on the order of 0.1 $\mu$N · s/m for a 60-$\mu$m-long cell (13,42,43). In this work, the damping coefficient of an outer hair cell ranges between 0.1 $\mu$N • s/m in the base and 0.25 $\mu$N · s/m in the apex.

For the nonstructural supporting cells (Hensen's, Claudius, and inner sulcus cells), the damping matrix was derived assuming that the material is isotropic and incompressible. The stress in the viscoelastic supporting cells depends on the strain and the strain rate or

$$\boldsymbol{\sigma} = \mathbf{D}\,\boldsymbol{\varepsilon} + \mathbf{D}'\dot{\boldsymbol{\varepsilon}}, \tag{13}$$

where the stress vector consists of normal stresses $\sigma_x$, $\sigma_y$, and $\sigma_z$ and shear stresses $\tau_{xy}$, $\tau_{yz}$, and $\tau_{zx}$, and the strain vector consists of the corresponding strains $\varepsilon_x$, $\varepsilon_y$, $\varepsilon_z$, $\gamma_{xy}$, $\gamma_{yz}$, and $\gamma_{zx}$. The elastic coefficient matrix $\mathbf{D}$ for an isotropic material can be found in continuum mechanics textbooks. Following Eskandari et al. (44), the viscous coefficient matrix $\mathbf{D}'$ is expressed in term of shear viscosity $\eta$ as

$$\mathbf{D}' = \frac{\eta}{3}\begin{bmatrix} 2 & -1 & -1 & 0 & 0 & 0 \\ -1 & 2 & -1 & 0 & 0 & 0 \\ -1 & -1 & 2 & 0 & 0 & 0 \\ 0 & 0 & 0 & 3 & 0 & 0 \\ 0 & 0 & 0 & 0 & 3 & 0 \\ 0 & 0 & 0 & 0 & 0 & 3 \end{bmatrix}. \tag{14}$$

The value of shear viscosity $\eta$ in this study is 42 mPa • s. Although there exist no measured results regarding the viscoelastic properties of the organ of Corti supporting cells, the shear viscosity of the tectorial membrane was measured to be between 110 and 260 mPa • s (45). The dissipation parameters are summarized in Table 2.

The mechanical parameters are summarized in Tables 1 and 2. To demonstrate how sensitive the model responses to different model parameters, additional results are presented in Figs. S1–S3 and S5.

## RESULTS

Typical model responses are presented in Fig. 3. The effect of fluid viscosity on cochlear mechanical gain is analyzed in Fig. 4. The contributions of different dissipating components are analyzed in Fig. 5. To investigate how model parameters affect cochlear power dissipation and to support our choice of key model parameters relevant to power dissipation, simulation results are compared with experimental measurements such as cochlear sensitivity change due to fluid viscosity (Fig. 4), tectorial membrane viscoelastic vibrations (Fig. 6), and cochlear input impedance (Fig. 7). A series of parametric studies shows the effects of model parameters on the cochlear input impedance (Fig. 8 *B*) and the tuning and amplification (Fig. 8). How dissipating properties affect the shape of the cochlear traveling waves is shown in Fig. 9.

**TABLE 2 Model Parameters: Dynamics**

| | Description | Property |
|---|---|---|
| $\rho$ | mass density (fluid and structures) | 1 g/cm$^3$ |
| $\mu$ | dynamic viscosity | $0.72 \times 10^{-3}$ Pa · s |
| $\alpha_C$ | damping coefficient (Eq. 11) | 0 s |
| $\beta_C$ | damping coefficient (Eq. 11) | $20 \times 10^3$ s$^{-1}$ |
| $c_{OHC}$ | outer-hair-cell damping coefficient per 10-$\mu$m section (base, apex) | $(0.3, 0.75) \times 10^{-6}$ N · s/m |
| $\eta$ | shear viscosity (Eq. 14) | $42 \times 10^{-3}$ P · s |

### Pure tone responses: Cochlear tuning and amplification

A general way to determine dissipating parameters for a cochlear model is to compare tuning and amplification characteristics with physiological observations. Representative model responses to pure tone stimulations are shown in Fig. 3. Several features commonly observed in physiological measurements are reproduced by our model. For example, the active responses are more sharply tuned and amplified than the passive responses (Fig. 3 *A*). The phase plots (*solid* and *broken curves*, Fig. 3 *A bottom panel*) share several characteristics with other experiments (46–48). First, near the best responding frequency, the phase slope of the active (sensitive) cochlea is steeper than the passive (insensitive) cochlea. Second, the phase-frequency curves of the passive and active cases cross each other near the best responding frequency. As a result of the first and second characteristics, before the crossing point, the phase of the passive case is greater than for the active case. The amplification and tuning quality are comparable to known values of the gerbil cochlea (Fig. 3 *B*, indicated with ▲) (46,49,50).

The trajectory of fluid particles depends on stimulating frequency. For high frequencies (Fig. 3 *C bottom*), fluid particle motions are circular, whereas for low frequencies (Fig. 3 *C top*), they are elliptical, elongated along the longitudinal direction. When passive, the maximal pressure amplitude occurs at the oval window. Note that according to experimental observations (51,52), the maximal pressure occurs near the peak location at the basilar membrane even for the high sound pressure level (SPL) stimulations. This implies that our "passive" condition is not equivalent to the physiological experiment at "high SPL." Alternatively, our 2-D fluid model may not accurately represent the 3-D nature of the scala fluid mechanics (53). When active, the maximal pressure occurs near the cochlear partition. This implies that the outer-hair-cell active feedback can overwhelm the input from the stapes (10,31).

### Primary power dissipation occurs within the OCC, not in the extra-OCC fluid

The effect of fluid viscosity on cochlear mechanics was simulated (Fig. 4). When the fluid viscosity was increased

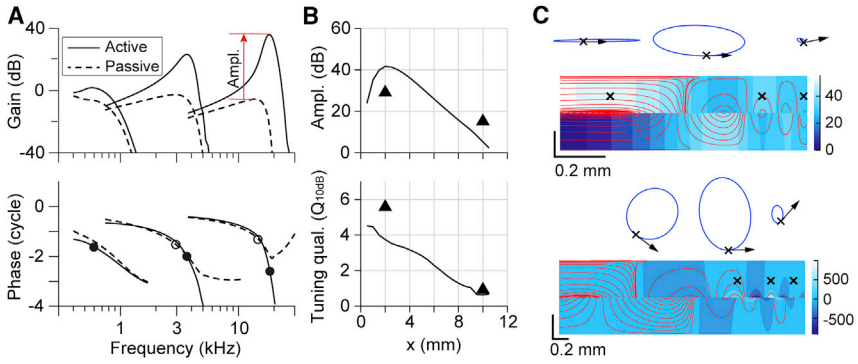


FIGURE 3 Pure tone responses. (*A*) Magnitude and phase of the basilar membrane displacement gain at $x = 10$, 6, and 2 mm are shown (*left* to *right*). The gain is with respect to the stapes displacement. Solid and broken curves are active and passive responses, respectively. The red arrow defines the amplification of this study. The filled and open circles in the phase plot indicates the phase at the peak locations for the active and passive cases, respectively. (*B*) Amplification level and tuning quality versus distance from the base are shown. The triangular symbols (▲) are measured data from others (46,49,50). (*C*) Pressure contours and particle traces resulting from the passive model subjected to 0.6 kHz stimulation (*top*) and the active model subjected to 18.3 kHz stimulation (*bottom*) are shown. The color bar indicates pressure level in mPa when the maximal inward velocity of the stapes is 1 $\mu$m/s.

to 10 times the standard value ($10\ \mu_{Std} = 7.2 \times 10^{-3}$ Pa · s), there was less than 5 dB change in the vibration amplitudes. The change in vibration amplitude exceeds 10 dB when the viscosity is greater than 30 times the standard value (Fig. 4 *B*). The effect of fluid viscosity was greater in the low-frequency locations.

These simulations are analogous to a recent experiment by Wang and Olson (54). In the experiment, they perfused

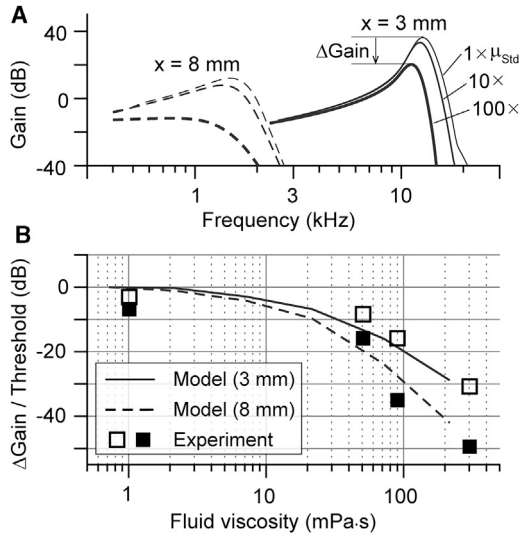


FIGURE 4 Effect of fluid viscosity. Different levels of fluid viscosity were simulated, and results were compared with experimental data (Wang and Olson, (54), their Fig. 3, *C* and *D*). (*A*) The basilar membrane displacement gain at $x = 8$ and 3 mm (active model) is shown. The three curves correspond to the model simulated with 1, 10, and 100 times the standard viscosity value ($\mu_{Std} = 0.72$ mPa · s). The change in gain ($\Delta$Gain) due to a 100 times increase in fluid viscosity is indicated with an arrow. (*B*) The change in the basilar membrane displacement gain due to viscosity change is presented together with the measured CAP threshold shift. The change of gain or threshold is presented in dB regarding gain or threshold at physiological condition ($\mu = \mu_{Std}$). An increased CAP threshold is presented as a decreased gain for comparison. At each viscosity level, we took the mean CAP threshold shift in the frequency range between 2 and 14 kHz. Different markers correspond to two sets of data (■: #483, □: #523).

viscous fluids into the scala tympani through the open round window. By making a small hole near the stapes for fluid withdrawal, they replaced the perilymph with testing fluids of different viscosities ranging between 1 and 500 mPa • s. They reported that the change in compound action potential (CAP) threshold is minimal at $\mu = 50$ mPa • s, but the CAP threshold was increased by 20–50 dB when $\mu = 300$ mPa • s. For comparison, their measured CAP threshold changes due to different fluid viscosity levels are shown together with our simulated mechanical gain change (Fig. 4 *B*). Both the experiment and our results suggest that for the extra-OCC fluid viscosity to affect the cochlear sensitivity, the viscosity must be 10 times or greater than the physiological level.

To investigate where the power dissipation occurs in the cochlea, the total power dissipation was divided into different components (Fig. 5). First, the total power dissipation is divided into the dissipation in the extra-OCC fluid domain and intra-OCC dissipation (or $P_{Total} = P_{fluid} + P_{OCC}$). Then, the intra-OCC dissipation is divided again into the dissipations in the tectorial and basilar membranes and in the organ of Corti (or $P_{OCC} = P_{TM,BM} + P_{OC}$). Intra-OCC dissipation is represented by $\mathbf{C}$, the damping matrix of the FE model, and occurs within cells and tissues of the OCC. Dissipated power is obtained from the rate of work done by the dissipating forces averaged over one cycle. Intra-OCC dissipated power is calculated from

$$P_{OCC} = 0.5\ \mathbf{v}_{OCC}^{CT}\ \mathbf{C}\ \mathbf{v}_{OCC}, \qquad (15)$$

where $\mathbf{v}_{OCC}$ is the OCC velocity vector. The superscript CT indicates conjugate-transpose. If only specific FE types such as the tectorial membrane and basilar membrane elements are chosen to assemble the $\mathbf{C}$ matrix, then Eq. 15 yields the dissipation in those elements.

Power dissipation in the extra-OCC fluid occurs mainly in the viscous boundary layers adjacent to the basilar and tectorial membranes because of the membrane oscillations. Power dissipated per cycle in the extra-OCC fluid is

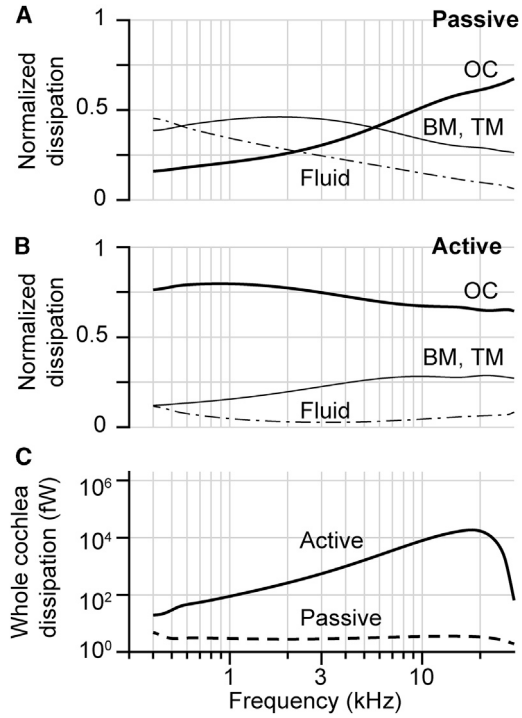


FIGURE 5 Power dissipation in the cochlea. The cochlear model was subjected to a series of pure tone simulations through the stapes (velocity amplitude of 1 $\mu$m/s regardless of frequency). The total dissipated power was divided into three components depending on where the dissipation occurs: extra-OCC in the scala fluid (Fluid) and intra-OCC in the OCC. Intra-OCC dissipation is divided into dissipation in the organ of Corti (OC) and in the basilar and tectorial membranes (BM and TM). The three components were normalized by the total dissipated power and plotted versus frequency for the (*A*) passive and (*B*) active cases. (*C*) Total power dissipation in the cochlea for the active and passive responses is shown.

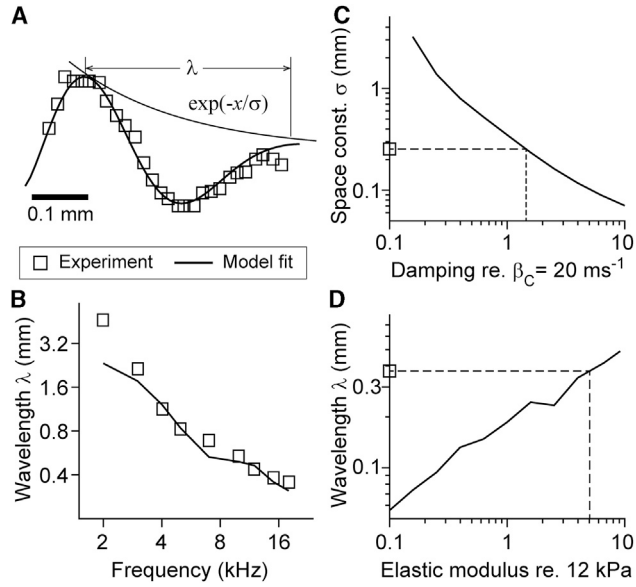


FIGURE 6 For a Figure360 author presentation of this figure, see https://doi.org/10.1016/j.bpj.2019.02.022. Figure360▷

Viscoelastic properties of the tectorial membrane. FE model of the tectorial membrane simulated the experiment of Ghaffari et al. (45). (*A*) The tectorial membrane model was subjected to radial vibrations at 15 kHz. The decaying space constant ($\sigma$) and the wavelength ($\lambda$) are determined by viscoelastic properties. (*B*) Wavelength is dependent on stimulating frequency. (*C*) Space constant is determined by damping property. The damping property was normalized with the standard value used in this work. (*D*) Wavelength varies depending on the elastic modulus of longitudinal elements. The broken lines in (*C*) and (*D*) indicate the value used to fit the experimental data. See text for simulation details.

calculated from the volume integral of the dissipation function $\phi$:

$$P_{Fluid} = \int\int \beta(x) b(x)\, \varphi(x,z)\, dxdz, \qquad (16)$$

where $b$ is the width of the basilar membrane and $\beta$ is the ratio between the widths of the fluid chamber and basilar membrane. The dissipation function is the power dissipation per unit volume, defined as

$$\varphi(x,z) = \mu\left(\frac{\partial \mathbf{u}}{\partial x}\frac{\partial \mathbf{u}}{\partial x}^{CT} + \frac{\partial \mathbf{v}}{\partial z}\frac{\partial \mathbf{v}}{\partial z}^{CT}\right) + \frac{\mu}{2}\left(\frac{\partial \mathbf{u}}{\partial z} + \frac{\partial \mathbf{v}}{\partial x}\right)\left(\frac{\partial \mathbf{u}}{\partial z} + \frac{\partial \mathbf{v}}{\partial x}\right)^{CT}. \qquad (17)$$

Most energy is dissipated within the OCC. Extra-OCC dissipation contribution became significant only when the passive cochlea vibrated at low frequencies (<2 kHz, Fig. 5 *A*).

There are several differences between the power dissipation patterns in the active and passive cochlear models. First, amplified vibrations in the active case result in greater power dissipation. When subjected to the same stapes velocity, the active cochlea dissipates orders of magnitude more power than the passive case (Fig. 5 *C*). This greater dissipation in the active case is ascribed to the increased vibration amplitude (up to 40 dB, Fig. 3 *B*). Second, unlike the passive case in which the total dissipation remained at a similar level over different stimulating frequencies, in the active case, the power dissipation increased as the stimulating frequency increases from 1 to 20 kHz. Third, the fraction of power dissipated in the organ of Corti (labeled as "OC" in Fig. 5, *A* and *B*) was greater when active. The increased dissipation of the active organ of Corti is ascribed to the increased deformation of the tissue because of outer-hair-cell motility.

It must be noted that our power dissipation analysis depends critically on model parameters, especially on the intra-OCC damping properties. Theoretical studies, including ours, chose the damping properties so that the model responses (amplification and tuning quality) become comparable to experimentally measured values. In the following, we show that our chosen damping properties are reasonable by comparing them with existing experiments and present how different damping values affect the model responses.

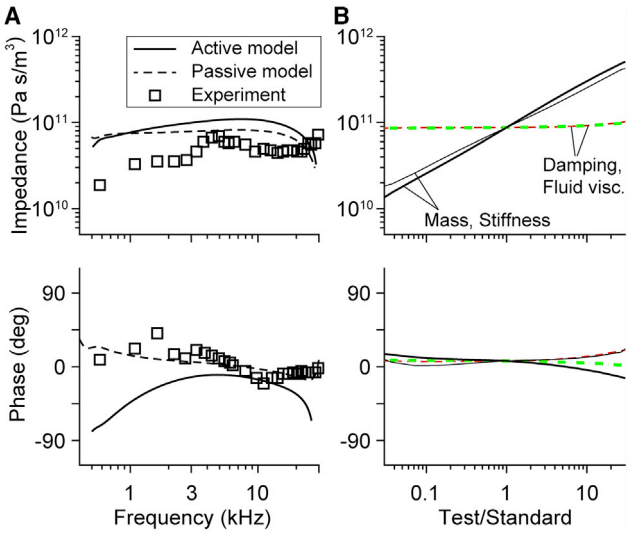


FIGURE 7 Cochlear input impedance. Simulated cochlear input impedance is shown together with the experimental results by de la Rochefoucauld et al. (8). In the experiment, intracochlear fluid pressure near the stapes and the stapes velocity were measured to obtain the input impedance. The same condition was simulated with our model. (*A*) Magnitude and phase of the cochlear input impedance are shown. (*B*) Cochlear input impedance of the passive cochlea at 3 kHz is shown as a function of normalized model parameters—damping, mass, and stiffness of the OCC and the fluid viscosity. The OCC mechanical properties were changed by multiplying the standard **K**, **C**, and **M** matrices (obtained using the parameters in Tables 1 and 2) by the Test/Standard ratio. To see this figure in color, go online.

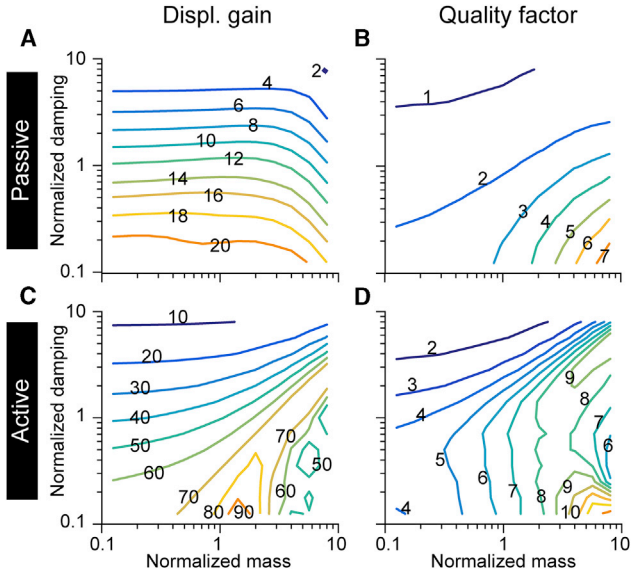


FIGURE 8 Effect of mass and damping properties on gain and tuning. The displacement gain (displacement ratio between the basilar membrane and the stapes) and tuning quality were obtained for different mass and damping properties for an 8 kHz pure tone. The numbers on the contour curves indicating the basilar membrane displacement gain regarding stapes are presented in dB, and the quality factor is computed according to Eq. 20. (*A*) Displacement gain, passive cochlea, is shown. (*B*) Tuning quality, passive cochlea, is shown. (*C*) Displacement gain, active cochlea, is shown. (*D*) Tuning quality, active cochlea, is shown. Although the damping contributions of different model components are formulated differently, all of them are assembled into the global **C** matrix. Therefore, to simulate different damping levels, a multiplication factor (*mf*) was applied to the matrix with standard properties ($\mathbf{C}_{Std}$), i.e., $\mathbf{C}_{Test} = mf \times \mathbf{C}_{Std}$. The same applies to the mass matrix.

## Comparing the viscoelastic response of the tectorial membrane with experiments

The viscoelastic responses of a section of the tectorial membrane were simulated and compared to experimental measurements to assess our choice of dissipation parameters. The tectorial membrane accounts for approximately a quarter of the cross-sectional area of the OCC (55). The viscoelastic responses of the tectorial membrane have been investigated for the mouse cochlea (45,56). Ghaffari and his colleagues applied sinusoidal stimulation to one end of the tectorial membrane section, excised from the mouse cochlea. From the vibrating patterns of the tissue, the wavelength and decaying space constant were measured.

The experimental results were reproduced with the tectorial membrane components of our model (Fig. 6). A 500-$\mu$m-long section of the tectorial membrane was simulated. The tectorial membrane model consists of beams running in the longitudinal and radial directions. The dynamics of the fluid surrounding the isolated tectorial membrane were not incorporated because the external fluid adds negligible inertia and viscous friction (57). As in the experiment, one short end of the tectorial membrane was subjected to time harmonic radial displacement, whereas the other end was fixed. The tectorial membrane formed propagating waves with amplitude decaying with distance from the excited edge. Three parameters determine the wavelength and decay space constant of the propagating waves ($\lambda$ and $\sigma$ in Fig. 6 *A*). They are the elastic modulus of longitudinally running elements, the damping, and the mass. The mass was the most reliable parameter because it was assigned using available anatomical data (1.4 $\mu$g for 1-mm section, estimated from a microscopic image in (58)). Simulated results fit the experimental data best when the Rayleigh damping coefficient $\beta_C$ was 34 ms$^{-1}$ and the elastic modulus of the longitudinal elements was 60 kPa (Fig. 6, *C* and *D*). For our gerbil cochlear model, the longitudinal element modulus was 12 kPa, and $\beta_C$ was 20 ms$^{-1}$. Our model was able to reproduce the wavelength change with frequency, using a constant value of $\beta_C$ that was independent of frequency (Fig. 6 *B*).

## Cochlear input impedance does not reflect how the energy is dissipated in the cochlea

A way of identifying dissipative and conservative parts of a physical system is to measure impedance: the complex ratio of applied force/response velocity. The real and imaginary parts of the impedance represent resistive (damping) and conservative (mass and stiffness) components of the system,

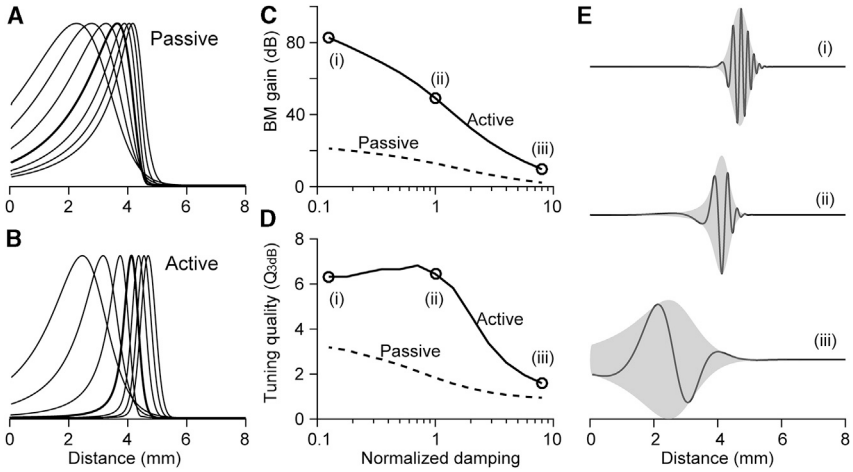


FIGURE 9 Optimal damping for tuning quality. Different damping levels were simulated. (*A*) Passive responses: normalized envelopes of the basilar membrane vibration when the model is subjected to 8 kHz sinusoidal stimulations. From the left to the right, the seven curves correspond to different damping levels of 1/8, 1/4, 1/2, **1**, 2, 4, and 8 times the standard value. The standard case was distinguished with a thicker line. (*B*) Active responses are shown. (*C*) The basilar membrane displacement gain with respect to the stapes is shown in dB. (*D*) Tuning quality along different damping levels is shown. (*E*) Traveling waves and envelopes for three different intra-OCC damping values of the active cochlea are shown. Top, middle, and bottom panels correspond to points labeled (*i*), (*ii*), and (*iii*) in (*C*) and (*D*).

respectively. The cochlear input impedance $Z_0$ is defined as the ratio of the pressure in the scala vestibuli near the stapes $p_0$ and the stapes volume velocity $U_0$,

$$Z_0 = p_0/U_0. \tag{18}$$

The volume velocity was obtained by multiplying the stapes velocity with the oval window area of 0.8 $mm^2$ (Mongolian gerbil cochlea, (59)). To investigate the dissipating and conservative components of the cochlea, the input impedance of our cochlear model was compared to the existing experimental data from de la Rochefoucauld and her colleagues (8) Fig. 7 *A*, and a series of parametric studies was performed, Fig. 7 *B*.

Overall, passive cochlear input impedance is in reasonable agreement with the measurement. Our magnitude remains relatively flat, in the range of 6–7 $\times$ $10^{10}$ Pa $\cdot$ $s/m^3$ in the 0.5–20 kHz range. Measured amplitude varies modestly (3–6 $\times$ $10^{10}$ Pa $\cdot$ $s/m^3$) in the same frequency range. Active cochlear input impedance is similar in amplitude to the passive but not as flat (it changes by a factor of 2). The difference in phase between the active and the passive cases is ascribed to the additional power source within the cochlea. That is, the power generated by the outer hair cells affects the fluid pressure opposing the oval window vibrations. The impedance was minimally affected by damping and fluid viscosity and was proportional to approximately the square root of stiffness and mass (Fig. 7 *B*), in agreement with the asymptotic estimation of Zwislocki (60). Zwislocki's asymptotic expression suggests that the cochlear input impedance is dominated by the effort to generate outgoing waves that propagate along the cochlear partition. Over most of the frequency range, these waves are essentially dissipated before reaching the helicotrema, so most of the wave energy is dissipated, and the reflected wave energy is typically negligible.

The conclusion of Fig. 7 is that the cochlear input impedance is different from mechanical impedance—the real part of the cochlear input impedance does not represent the dissipation of the system. We abstain from making further conclusions from this result because of some simplifications of our fluid mechanical model. The cochlear input impedance is measured at the basal extreme where the fluid space is 3-D (the depth and width of the scala are not negligible compared to the length). The cochlea is coiled with a smaller radius of curvature and tapered toward the apex. Because our 2-D rectangular fluid domain may not represent the basal or apical fluid dynamics accurately, the model could miss fine characteristics of the cochlear input impedance, especially near the high-frequency end (>25 kHz) and low-frequency end (<0.5 kHz). Indeed, other theoretical studies demonstrated that the fine characteristics of the cochlear input impedance are better reproduced when the more realistic scalar fluid dynamics are considered, such as tapered scalae and realistic helicotrema (61,62).

Another study by Dong and Olson (63) was dedicated to OCC mechanical impedance. They measured the fluid pressure and the basilar membrane vibration simultaneously from live gerbils to estimate the OCC mechanical impedance. Because the measurements were made more than an octave below the CF of the measured location, as the authors stated, the impedance is elastic rather than resistive (dissipating). Our simulation results compare well with the measurements in that 1) the amplitude is comparable—our acoustic stiffness at $x$ = 0.5 mm 4 GPa/m is within the measured range of 2.5–12 GPa/m; 2) the impedance phase is ~90°; and 3) there is little difference between the active (their low SPL case) and the passive (their postmortem case) impedance (Fig. S6).

## Existence of equivalent parameter set with reduced mass and damping

There may exist equivalent parameter sets resulting in the same cochlear performance in tuning quality and amplification. For instance, according to vibration theory

for an underdamped mechanical system, the tuning quality is inversely related to the damping factor $\varsigma$ or $Q_{3dB} \approx 0.5/\varsigma = 0.5\sqrt{mk}/c$, where the $c$, $m$, and $k$ represent the damping, mass, and stiffness of the system, respectively. It is possible that the organ of Corti tissue or the tectorial membrane is so soft that they behave more like a fluid than a solid or that the OCC mass is negligible. Indeed, there are studies that neglected the effect of OCC inertia (26,64). Had we overestimated the OCC mass so that structural mass became more dominant than extra-OCC fluid inertia, the intra-OCC damping property could be overestimated as well.

We investigated the effect of intra-OCC damping and mass on the amplification and sharpness of tuning. Because our model has better spatial than frequency resolution, the tuning quality in this section was obtained from the spatial envelope of traveling waves by using local scaling symmetry in the cochlea (19). According to Greenwood's frequency map (65), the characteristic frequency (CF) at a location $x$ can be represented by a logarithmic function such as

$$CF(x) = a\ \left(10^{(L-x)/b} - c\right), \tag{19}$$

where the coefficients for the gerbil cochlea are $a = 0.4$ kHz, $b = 5.75$ mm, $L = 12$ mm, and $c = 0.85$. When the span of the traveling wave envelope 3 dB below the peak is $x_1 < x < x_2$, we defined the quality factor at $x$ as

$$q_{3dB}(x) = CF(x)/(CF(x_1) - CF(x_2)). \tag{20}$$

This spatially defined tuning quality is comparable to the conventional tuning quality obtained from frequency-gain curves (Fig. S7).

The level of amplification is defined as the amplitude ratio between active and passive peak responses at the location of interest. Fig. 8 shows the tuning quality and amplification as a function of changing mass and damping of the model.

Regarding the relationship between the mass or damping and the amplitude gain or tuning quality, our passive cochlear model is consistent with simple vibration theory, but the active model is not. In the active model, decreasing the damping does not necessarily increase the tuning quality. In the series of simulations (Fig. 8), the mass and intra-OCC damping were varied over two orders of magnitude from the standard values used in this work. When passive, the model cochlea follows simple vibration theory—both the tuning quality and the displacement gain vary monotonically as shown in Fig. 8, *A* and *B*. However, when the cochlea becomes active (Fig. 8, *C* and *D*), the modeled cochlear responses clearly contrast with the passive responses—both along the mass and along the damping axes, the tuning and amplification do not vary monotonically.

## Can dissipation enhance tuning quality?

A parametric study of the intra-OCC damping clearly reveals a difference between passive and active cochlear mechanics (Fig. 9). With all other model parameters fixed, only the intra-OCC damping was changed over two orders of magnitude about the standard value. When passive (Fig. 9 *A*), as the damping increases, the width of the traveling wave envelope increases, corresponding to a decreasing quality factor (*broken curves* in Fig. 9, *C* and *D*). However, when the cochlea is active (Fig. 9 *B*), the tuning versus damping relationship is not monotonic (*solid curves* in Fig. 9, *C* and *D*). As the intra-OCC damping increases, the width of the traveling wave envelope peaks at a certain damping level (Fig. 9 *C*). That is, our study predicts that there exists an optimal intra-OCC damping for the best tuning quality (Fig. 9 *D*).

The effect of intra-OCC damping on the traveling wave in the active cochlea is further demonstrated in Fig. 9 *E*. As the damping increases, the wavelength of the traveling wave increases. For example, as the damping level increased by a factor of eight from (*i*) to (*ii*) and to (*iii*), the wavelength near the peak increased from 200 to 380 $\mu$m and to 1800 $\mu$m. On the other hand, as the damping level increases, the number of wave cycles decreases. For the three cases of (*i*), (*ii*), and (*iii*), the number of wave cycles decreased from 10 to 4 and to 2. As damping level varies, these two factors (wavelength and number of waves) compete to determine the width of the wave envelope. Our results demonstrate that there exists a damping level range that results in the maximal tuning. With the standard damping value of this study, case (*ii*), the wavelength is comparable to physiologically observed values, whereas the number of cycles is greater by 1–2 cycles (66).

The difference between the passive and the active cases originates from different modes of acoustic energy transmission. In the passive case, the acoustic energy enters at the oval window and dissipates monotonically toward the apex. At reduced intra-OCC damping, the energy travels further or, from the point of view of a fixed location, the best responding frequency increases and wavelength gets shorter. In the active case, in addition to the acoustic input at the stapes, the energy is generated within the organ of Corti. This generated energy can be much greater than the input energy (10). The streamline patterns and pressure field in Fig. 3 *C* show this energy flow. In the passive case (*top panel*), the greatest pressure amplitude occurs at the oval window ($x = 0$). However, in the active case (*bottom panel*), the greatest pressure amplitude is at the best responding site.

The intra-OCC dissipation has two contradictory effects. First, it opposes the active power generation. Second, it stops the spreading of the energy away from the generation site. Until a certain level of intra-OCC damping is reached, the latter role (stopping the spreading) is more prominent so that the tuning quality increases as the intra-OCC damping increases. However, above the optimal value, the intra-OCC

damping begins to suppress the active power generation itself.

## DISCUSSION

The conclusion of this study is that an appropriate level of damping can enhance the tuning quality when the cochlea is active (Figs. 8 and 9). The other conclusion of this study is that the majority of acoustic power in the cochlea is dissipated within the OCC rather than in the scala fluid (Figs. 4 and 5). The dissipation in the viscous scala fluid becomes comparable to the OCC dissipation only when the passive cochlea is subjected to low-frequency stimulations (<2 kHz). As a result, cochlear amplification and tuning are minimally affected by the viscosity of the extra-OCC fluid. To justify the choice of OCC damping properties, we compared viscoelastic responses of the tectorial membrane with experimental results (Fig. 6). Both the comparison with the measured data and the parametric study suggest that the OCC damping properties of this study are reasonable. In the following, we discuss the damping properties in the literature and present several first-order approximations of different dissipating mechanisms.

### Damping properties in the literature

Damping properties used in different theoretical studies are summarized in Table 3. Nearly all other studies used fewer degrees of freedom to represent the cochlear mechanics than used in our study, but all models have a degree of freedom representing the transverse displacement of the basilar membrane. Therefore, for the sake of comparison, our OCC damping was converted to an effective damping coefficient with respect to the basilar membrane vibrations. The effective damping coefficient of the OCC per 10-$\mu$m-long cross section is computed from the dissipated power within the section, $\Delta P_{OCC}$, and the basilar membrane velocity, $\mathbf{v}_{BM}$, as

$$c_{OCC} = 2\Delta P_{OCC}/\mathbf{v}_{BM}^{CT}\mathbf{v}_{BM}. \quad (21)$$

**TABLE 3 Damping Coefficients in the Literature**

| Reference | Case: Base, Apex | Species |
|---|---|---|
| Neely and Kim (21) | BM: 15, 0.3; TM: 0.1, 0.0004; OC: 0.02, 0.003 | cat |
| Diependaal et al. (22) | 5, 0.03 | human |
| Mammano and Nobili (23) | 1.6, 0.38 | guinea pig |
| Kolston and Ashmore (20) | BM: 2.0; TM: ~17–170 | human |
| Lu et al. (24) | BM: 1.9, 13; RL: 0.5, 3.5 | guinea pig |
| Liu and Neely (25) | 15, 86 | human |
| Meaud and Grosh (81) | BM: 0.85, 0.43; TM: 1.5, 0.75 | guinea pig |
| This study | passive: 2.2 to 0.23; active: 7.5–0.92 | gerbil |

Unit in (kN · s/m$^3$). BM, basilar membrane; OC, organ of Corti; TM, tectorial membrane; RL, reticular lamina.

Note that, because this "effective" property is dependent on vibration patterns, the value is dependent on vibrating frequency and active outer-hair-cell feedback. When passive (i.e., when all the elements in the cross section vibrate approximately in phase), the values of $c_{OCC}$ range from 3.5 $\mu$N · s/m at the base to 0.64 $\mu$N · s/m at the apex. When considered per unit basilar membrane area, these values correspond to 2.2 and 0.23 kN · s/m/m$^2$. When active, increased relative (out-of-phase) motion within the organ of Corti increases overall dissipation. As a result, when active, the value of $c_{OCC}$ increases to 12 $\mu$N · s/m at the base and to 2.6 $\mu$N · s/m at the apex.

As summarized in Table 3, theoretical studies have used a wide range of dissipating properties. Some studies used greater damping value toward the base, whereas others considered the opposite trend. In a model not included in the table (10), the intra-OCC damping was not incorporated. Instead, they incorporated fluid viscosity as the dissipating mechanism. It is clear that a consensus does not exist for dissipating properties of the cochlea. Considering that the dissipating property is crucial to reconcile different hypothetical mechanisms of cochlear amplification, more quantitative experimental data regarding the organ of Corti viscoelastic responses will be very valuable in settling current debates on the operating mechanisms of cochlear mechano-transduction.

Existing experiments are consistent with our conclusion that the extra-OCC fluids are not the medium through which most cochlear acoustic energy is dissipated. Wang and Olson (54) replaced the perilymph of the cochlea with fluids with higher viscosity. They showed that the cochlear sensitivity was compromised when the fluid viscosity level was increased by more than 50 times the physiological value. This implies that the cochlear mechanics is hardly affected by the extra-OCC fluid viscosity under physiological condition. This is reasonable only if the dominant dissipating factor is not the extra-OCC fluids. Indeed, Freeman and his colleagues measured the effective viscosity of the tectorial membrane to be about two orders of magnitude greater than the extra-OCC fluids (45,56,57). This observation is in agreement with Wang and Olson's—the extra-OCC fluid viscosity must be increased by two orders of magnitude to affect the cochlear sensitivity (to become a dominant mechanism for energy dissipation). When considered in terms of an effective fluid viscosity, our OCC FEs have an effective viscosity between 10 and 100 times that of the extra-OCC fluids.

### The legitimacy of using the Rayleigh damping

In rheological studies on biological tissues, the complex shear modulus is expressed as $G(\omega) = G'(\omega) + i\omega G''(\omega)$, where the storage modulus $G'$ and the loss modulus $G''$ are dependent on the frequency ($\omega$). According to the power-law damping model (67), the loss (imaginary) term

is divided into two components so that the complex shear modulus can be written as $G = G_0(1 + i\eta)(\omega/\omega_0)^{\alpha}\Gamma(1 - \alpha)\cos(\pi\alpha/2) + i\omega\mu$. Here, $G_0$ is the static shear modulus, $\alpha$ defines the power law that represents the frequency dependence of the elastic and structural dissipation components, $\omega_0$ is a scale factor for the frequency, and $\Gamma$ denotes the gamma function. Often, $\alpha$ is small, and in such cases, $\Gamma(1 - \alpha)\cos(\pi\alpha/2)$ becomes close to unity. Two imaginary terms constitute $G''$: the term including $\eta$ is called the structural (frictional) damping, and the term including $\mu$ is called the Newtonian viscous damping. When cytoskeletal structures are subject to vibrations >100 Hz, the viscous (Newtonian) stress is dominant as compared to the frictional stress (68–70). Even at low frequencies, the frictional stress is confined within the densely organized structures of cytoskeleton (71–74). Although most rheological tests with biological tissues/cells were done at below 100 Hz, at which the frictional term is not negligible, the cochlear epithelium vibrates at kHz range. Therefore, in the cochlear mechanics, the dissipation must be dominantly viscous rather than frictional.

The Rayleigh damping that we used ($i\omega\beta_C\mathbf{M}$) is equivalent to the Newtonian loss term ($i\omega\mu$) or $\beta_C\mathbf{M}$ is equivalent to $\mu$, and the structural damping term is neglected. Note that the mass matrix $\mathbf{M}$ is just used to form a damping matrix for the FE formulation, but it does not imply that the viscous damping is proportional to inertia. Consistent with the viscous (Newtonian) loss theory, the Rayleigh damping model reproduced the frequency-dependent response with constant $\beta_C$ (Fig. 6 *B*).

## Limitations of the model

Cochlear mechanics is nonlinear as a consequence of the nonlinear mechanotransduction. The cochlear nonlinearity has been considered in studies in which the nonlinearity is central to their subject, such as otoacoustic emissions (25,75) and two-tone suppressions (32). On the other hand, most other studies have used linearized models because a nonlinear model is computationally expensive and prone to stability issues. The implicit assumption of our model is that intrinsic mechanical properties such as the structural mass, stiffness, and damping properties do not depend on cochlear nonlinearity. In reality, however, the active feedback of the outer hair cell can serve as an effective mass, stiffness, or damping, and the feedback is level dependent. In linearized models, the active feedback is linearized to represent the "most sensitive" cochlea. Therefore, linearized cochlear models including ours approximate either the sensitive cochlea (i.e., response to small sounds) or insensitive cochlea (i.e., response of postmortem cochlea) but cannot accurately predict level-dependent responses. It has been thought that the cochlear responses to loud sound (>80 dB sound pressure level) are close to the postmortem case, but recent results seem not congruent with the view (47).

## Origin of power dissipation in the OCC: Rough estimation of OCC damping

Although it is difficult to make an accurate estimation of OCC damping, at least potential dissipating mechanisms within the OCC can be discussed. In the following, three mechanisms are listed—the dissipation in the subtectorial space, the dissipation due to fluid flow within the organ of Corti, and the dissipation in viscoelastic cells.

First, the subtectorial space (the micrometer-thick fluid layer between the tectorial membrane and the reticular lamina) has been considered to be a major location for energy dissipation (23). If the subtectorial space is represented with a fluid layer between a pair of parallel plates, the damping coefficient is determined by the viscosity and geometry as $c_{STS} = \mu Lw/h$, where $L$, $w$, and $h$ are the length, width, and height of the space. The value may range between 0.1 and 1 $\mu$N · s/m for a length of $L = 10$ $\mu$m (the longitudinal spacing between outer hair cells). In our recent study (16), it was shown that this dissipation in the subtectorial space can further increase at low frequencies because of the additional viscous friction of the inner-hair-cell stereocilia bundle. In this work, we incorporated only the simplistic parallel plate estimations ($c_{STS}$). Therefore, the damping in the subtectorial space could be underestimated, especially for low stimulating frequencies.

Second, deformation of the organ of Corti due to outer-hair-cell motility may induce viscous friction. Recent measurements (47,76) clearly demonstrated that there exists considerable out-of-phase motion between the top and bottom surfaces of the organ of Corti. This deformation may be substantial enough to induce longitudinal fluid flow along the tunnel of Corti (77). According to the mechanical impedance of the pulsating flow of viscous fluid in a pipe (78), the effective damping coefficient along the tunnel of Corti can be approximated with $c_{TC} = \pi rL\sqrt{2\mu\rho\omega}$, where $r$ is the effective radius of the tube. Considering the geometry and best frequency of different locations, the estimated damping coefficient will be a fraction of 1 $\mu$N • s/m for a length of $L = 10$ $\mu$m. This value will define a lower limit because there must be other fluid motion within the organ of Corti besides the longitudinal flow along the tunnel of Corti.

Finally, deforming viscoelastic cells in the organ of Corti will dissipate power. In particular, the outer hair cells themselves must deform because of their electromotility. The axial damping coefficient of an outer hair cell was estimated to be on the order of 0.1 $\mu$N · s/m for a 60-$\mu$m-long cell (13). Considering three rows of outer hair cells, this corresponds to $c_{OHC} = 0.3$ $\mu$N · s/m per 10-$\mu$m section.

These three damping coefficients correspond to different motions—subtectorial space shear velocity, longitudinal fluid flow in the tunnel of Corti, and cellular deformations in the organ of Corti. Therefore, for better comparison with those values in Table 1, they need to be converted with pertinent kinematic factors relating to the basilar membrane

velocity. Based on available evidence, the kinematic factors seem not far from unity. For example, the stereocilia bundle displacement that equals the subtectorial space shear displacement and the outer-hair-cell somatic deformation are comparable to the basilar membrane displacement (30,36,47,79). Although our model incorporated the subtectorial space damping and the outer-hair-cell damping explicitly, the dissipation due to the tunnel of Corti fluid flow was not considered explicitly in this model.

These rough estimations are on the order of 1 $\mu$N $\cdot$ s/m per 10-$\mu$m section, supporting our conclusions that the major power dissipating place in the cochlea is the OCC and that the power dissipation depends on vibration modes of the OCC modulated by the outer-hair-cell motility.

## SUPPORTING MATERIAL

Supporting Material can be found with this article online at https://doi.org/10.1016/j.bpj.2019.02.022.

## AUTHOR CONTRIBUTIONS

S.P. and J.-H.N. conceived the research. S.P. and J.-H.N. wrote and ran the computer programs. S.P., S.M.G., and J.-H.N. analyzed the data and wrote the manuscript.

## ACKNOWLEDGMENTS

This work was supported by National Institutes of Health NIDCD R01 DC014685.

## REFERENCES

1. Olson, E. S., H. Duifhuis, and C. R. Steele. 2012. Von Békésy and cochlear mechanics. *Hear. Res.* 293:31–43.
2. Gold, T. 1948. Hearing. 2. The physical basis of the action of the cochlea. *Proc. R Soc. Ser. B-Bio.* 135:492–498.
3. Ashmore, J. 2008. Cochlear outer hair cell motility. *Physiol. Rev.* 88:173–210.
4. Hallworth, R. 1995. Passive compliance and active force generation in the guinea pig outer hair cell. *J. Neurophysiol.* 74:2319–2328.
5. Iwasa, K. H., and M. Adachi. 1997. Force generation in the outer hair cell of the cochlea. *Biophys. J.* 73:546–555.
6. Overstreet, E. H., III, A. N. Temchin, and M. A. Ruggero. 2002. Basilar membrane vibrations near the round window of the gerbil cochlea. *J. Assoc. Res. Otolaryngol.* 3:351–361.
7. Puria, S. 2003. Measurements of human middle ear forward and reverse acoustics: implications for otoacoustic emissions. *J. Acoust. Soc. Am.* 113:2773–2789.
8. de la Rochefoucauld, O., W. F. Decraemer, …, E. S. Olson. 2008. Simultaneous measurements of ossicular velocity and intracochlear pressure leading to the cochlear input impedance in gerbil. *J. Assoc. Res. Otolaryngol.* 9:161–177.
9. Ramamoorthy, S., and A. L. Nuttall. 2012. Outer hair cell somatic electromotility in vivo and power transfer to the organ of Corti. *Biophys. J.* 102:388–398.
10. Wang, Y., C. R. Steele, and S. Puria. 2016. Cochlear outer-hair-cell power generation and viscous fluid loss. *Sci. Rep.* 6:19475.
11. Tolomeo, J. A., and C. R. Steele. 1998. A dynamic model of outer hair cell motility including intracellular and extracellular fluid viscosity. *J. Acoust. Soc. Am.* 103:524–534.
12. Rabbitt, R. D., S. Clifford, …, W. E. Brownell. 2009. Power efficiency of outer hair cell somatic electromotility. *PLoS Comput. Biol.* 5:e1000444.
13. Liao, Z., A. S. Popel, …, A. A. Spector. 2005. Modeling high-frequency electromotility of cochlear outer hair cell in microchamber experiment. *J. Acoust. Soc. Am.* 117:2147–2157.
14. Iwasa, K. H. 2016. Energy output from a single outer hair cell. *Biophys. J.* 111:2500–2511.
15. Steele, C. R., and S. Puria. 2005. Force on inner hair cell cilia. *Int. J. Solids Struct.* 42:5887–5904.
16. Prodanovic, S., S. Gracewski, and J. H. Nam. 2015. Power dissipation in the subtectorial space of the mammalian cochlea is modulated by inner hair cell stereocilia. *Biophys. J.* 108:479–488.
17. Ramamoorthy, S., N. V. Deo, and K. Grosh. 2007. A mechano-electro-acoustical model for the cochlea: response to acoustic stimuli. *J. Acoust. Soc. Am.* 121:2758–2773.
18. Lamb, J. S., and R. S. Chadwick. 2011. Dual traveling waves in an inner ear model with two degrees of freedom. *Phys. Rev. Lett.* 107:088101.
19. Shera, C. A. 2007. Laser amplification with a twist: traveling-wave propagation and gain functions from throughout the cochlea. *J. Acoust. Soc. Am.* 122:2738–2758.
20. Kolston, P. J., and J. F. Ashmore. 1996. Finite element micromechanical modeling of the cochlea in three dimensions. *J. Acoust. Soc. Am.* 99:455–467.
21. Neely, S. T., and D. O. Kim. 1986. A model for active elements in cochlear biomechanics. *J. Acoust. Soc. Am.* 79:1472–1480.
22. Diependaal, R. J., H. Duifhuis, …, M. A. Viergever. 1987. Numerical methods for solving one-dimensional cochlear models in the time domain. *J. Acoust. Soc. Am.* 82:1655–1666.
23. Mammano, F., and R. Nobili. 1993. Biophysics of the cochlea: linear approximation. *J. Acoust. Soc. Am.* 93:3320–3332.
24. Lu, T. K., S. Zhak, …, R. Sarpeshkar. 2006. Fast cochlear amplification with slow outer hair cells. *Hear. Res.* 214:45–67.
25. Liu, Y. W., and S. T. Neely. 2010. Distortion product emissions from a cochlear model with nonlinear mechanoelectrical transduction in outer hair cells. *J. Acoust. Soc. Am.* 127:2420–2432.
26. Lim, K. M., and C. R. Steele. 2002. A three-dimensional nonlinear active cochlear model analyzed by the WKB-numeric method. *Hear. Res.* 170:190–205.
27. Yoon, Y. J., C. R. Steele, and S. Puria. 2011. Feed-forward and feedbackward amplification model from cochlear cytoarchitecture: an interspecies comparison. *Biophys. J.* 100:1–10.
28. Motallebzadeh, H., J. A. M. Soons, and S. Puria. 2018. Cochlear amplification and tuning depend on the cellular arrangement within the organ of Corti. *Proc. Natl. Acad. Sci. USA.* 115:5762–5767.
29. Nam, J. H., Y. Liu, and S. M. Gracewski. 2014. A computational study on traveling waves in the gerbil cochlea generated by electrical impulse. *In* Mechanics of Hearing 12th International Workshop. D. Corey and K. D. Karavitaki, eds. American Institute of Physics.
30. Liu, Y., S. M. Gracewski, and J. H. Nam. 2015. Consequences of location-dependent organ of corti micro-mechanics. *PLoS One.* 10:e0133284.
31. Liu, Y., S. M. Gracewski, and J. H. Nam. 2017. Two passive mechanical conditions modulate power generation by the outer hair cells. *PLoS Comput. Biol.* 13:e1005701.
32. Meaud, J., and K. Grosh. 2014. Effect of the attachment of the tectorial membrane on cochlear micromechanics and two-tone suppression. *Biophys. J.* 106:1398–1405.
33. Cormack, J., Y. Liu, …, S. M. Gracewski. 2015. Two-compartment passive frequency domain cochlea model allowing independent fluid

coupling to the tectorial and basilar membranes. *J. Acoust. Soc. Am.* 137:1117–1125.

34. Dong, W., and E. S. Olson. 2016. Two-tone suppression of simultaneous electrical and mechanical responses in the cochlea. *Biophys. J.* 111:1805–1815.
35. Nam, J. H., and R. Fettiplace. 2010. Force transmission in the organ of Corti micromachine. *Biophys. J.* 98:2813–2821.
36. Nam, J. H., and R. Fettiplace. 2012. Optimal electrical properties of outer hair cells ensure cochlear amplification. *PLoS One.* 7:e50572.
37. Nam, J. H. 2014. Microstructures in the organ of Corti help outer hair cells form traveling waves along the cochlear coil. *Biophys. J.* 106:2426–2433.
38. Beurg, M., J. H. Nam, …, R. Fettiplace. 2008. The actions of calcium on hair bundle mechanics in mammalian cochlear hair cells. *Biophys. J.* 94:2639–2653.
39. Nam, J. H., and R. Fettiplace. 2008. Theoretical conditions for high-frequency hair bundle oscillations in auditory hair cells. *Biophys. J.* 95:4948–4962.
40. Howard, J., and A. J. Hudspeth. 1988. Compliance of the hair bundle associated with gating of mechanoelectrical transduction channels in the bullfrog's saccular hair cell. *Neuron.* 1:189–199.
41. Allen, J. B. 1980. Cochlear micromechanics–a physical model of transduction. *J. Acoust. Soc. Am.* 68:1660–1670.
42. Fleischer, M., C. Harasztosi, …, A. W. Gummer. 2011. Continuum mechanical model of the outer hair cell. *AIP Conference Proceedings.* 1403:160–165.
43. Ó Maoiléidigh, D., and A. J. Hudspeth. 2013. Effects of cochlear loading on the motility of active outer hair cells. *Proc. Natl. Acad. Sci. USA.* 110:5474–5479.
44. Eskandari, H., S. E. Salcudean, …, J. Ohayon. 2008. Viscoelastic characterization of soft tissue from dynamic finite element models. *Phys. Med. Biol.* 53:6569–6590.
45. Ghaffari, R., A. J. Aranyosi, and D. M. Freeman. 2007. Longitudinally propagating traveling waves of the mammalian tectorial membrane. *Proc. Natl. Acad. Sci. USA.* 104:16510–16515.
46. Ren, T., and A. L. Nuttall. 2001. Basilar membrane vibration in the basal turn of the sensitive gerbil cochlea. *Hear. Res.* 151:48–60.
47. Ren, T., W. He, and D. Kemp. 2016. Reticular lamina and basilar membrane vibrations in living mouse cochleae. *Proc. Natl. Acad. Sci. USA.* 113:9910–9915.
48. Chen, F., D. Zha, …, A. L. Nuttall. 2011. A differentially amplified motion in the ear for near-threshold sound detection. *Nat. Neurosci.* 14:770–774.
49. Temchin, A. N., and M. A. Ruggero. 2010. Phase-locked responses to tones of chinchilla auditory nerve fibers: implications for apical cochlear mechanics. *J. Assoc. Res. Otolaryngol.* 11:297–318.
50. Cooper, N. P., and W. S. Rhode. 1995. Nonlinear mechanics at the apex of the guinea-pig cochlea. *Hear. Res.* 82:225–243.
51. Olson, E. S. 1998. Observing middle and inner ear mechanics with novel intracochlear pressure sensors. *J. Acoust. Soc. Am.* 103:3445–3463.
52. Olson, E. S. 2001. Intracochlear pressure measurements related to cochlear tuning. *J. Acoust. Soc. Am.* 110:349–367.
53. Taber, L. A., and C. R. Steele. 1981. Cochlear model including three-dimensional fluid and four modes of partition flexibility. *J. Acoust. Soc. Am.* 70:426–436.
54. Wang, Y., and E. S. Olson. 2016. Cochlear perfusion with a viscous fluid. *Hear. Res.* 337:1–11.
55. Edge, R. M., B. N. Evans, …, P. Dallos. 1998. Morphology of the unfixed cochlea. *Hear. Res.* 124:1–16.
56. Ghaffari, R., A. J. Aranyosi, …, D. M. Freeman. 2010. Tectorial membrane travelling waves underlie abnormal hearing in Tectb mutant mice. *Nat. Commun.* 1:96.
57. Sellon, J. B., R. Ghaffari, and D. M. Freeman. 2017. Geometric requirements for tectorial membrane traveling waves in the presence of cochlear loads. *Biophys. J.* 112:1059–1062.
58. Cheatham, M. A., R. J. Goodyear, …, G. P. Richardson. 2014. Loss of the tectorial membrane protein CEACAM16 enhances spontaneous, stimulus-frequency, and transiently evoked otoacoustic emissions. *J. Neurosci.* 34:10325–10338.
59. Cohen, Y. E., C. K. Bacon, and J. C. Saunders. 1992. Middle ear development. III: morphometric changes in the conducting apparatus of the Mongolian gerbil. *Hear. Res.* 62:187–193.
60. Zwislocki, J. 1965. Analysis of some auditory characteristics. *In* Handbook of Mathematical Psychology. R. Luce, R. Bush, and E. Galanter, eds. John Wiley & Sons, pp. 1–97.
61. Shera, C. A., and G. Zweig. 1991. A symmetry suppresses the cochlear catastrophe. *J. Acoust. Soc. Am.* 89:1276–1289.
62. Puria, S., and J. B. Allen. 1991. A parametric study of cochlear input impedance. *J. Acoust. Soc. Am.* 89:287–309.
63. Dong, W., and E. S. Olson. 2009. In vivo impedance of the gerbil cochlear partition at auditory frequencies. *Biophys. J.* 97:1233–1243.
64. van der Heijden, M. 2014. Frequency selectivity without resonance in a fluid waveguide. *Proc. Natl. Acad. Sci. USA.* 111:14548–14552.
65. Greenwood, D. D. 1990. A cochlear frequency-position function for several species–29 years later. *J. Acoust. Soc. Am.* 87:2592–2605.
66. Ren, T. 2002. Longitudinal pattern of basilar membrane vibration in the sensitive cochlea. *Proc. Natl. Acad. Sci. USA.* 99:17101–17106.
67. Smith, B. A., B. Tolloczko, …, P. Grütter. 2005. Probing the viscoelastic behavior of cultured airway smooth muscle cells with atomic force microscopy: stiffening induced by contractile agonist. *Biophys. J.* 88:2994–3007.
68. Puig-de-Morales-Marinkovic, M., K. T. Turner, …, S. Suresh. 2007. Viscoelasticity of the human red blood cell. *Am. J. Physiol. Cell Physiol.* 293:C597–C605.
69. Rother, J., H. Nöding, …, A. Janshoff. 2014. Atomic force microscopy-based microrheology reveals significant differences in the viscoelastic response between malign and benign cell lines. *Open Biol.* 4:140046.
70. Alcaraz, J., L. Buscemi, …, D. Navajas. 2003. Microrheology of human lung epithelial cells measured by atomic force microscopy. *Biophys. J.* 84:2071–2079.
71. Fredberg, J. J., and D. Stamenovic. 1989. On the imperfect elasticity of lung tissue. *J. Appl. Physiol.* 67:2408–2419.
72. Sollich, P. 1998. Rheological constitutive equation for a model of soft glassy materials. *Phys. Rev. E Stat. Phys. Plasmas Fluids Relat. Interdiscip. Topics.* 58:738–759.
73. Maksym, G. N., B. Fabry, …, J. J. Fredberg. 2000. Mechanical properties of cultured human airway smooth muscle cells from 0.05 to 0.4 Hz. *J. Appl. Physiol.* 89:1619–1632.
74. Fabry, B., G. N. Maksym, …, J. J. Fredberg. 2001. Scaling the microrheology of living cells. *Phys. Rev. Lett.* 87:148102.
75. Wen, H., T. Bowling, and J. Meaud. 2018. Investigation of the $2f_1$-$f_2$ and $2f_2$-$f_1$ distortion product otoacoustic emissions using a computational model of the gerbil ear. *Hear. Res.* 365:127–140.
76. Lee, H. Y., P. D. Raphael, …, J. S. Oghalai. 2015. Noninvasive in vivo imaging reveals differences between tectorial membrane and basilar membrane traveling waves in the mouse cochlea. *Proc. Natl. Acad. Sci. USA.* 112:3128–3133.
77. Karavitaki, K. D., and D. C. Mountain. 2007. Evidence for outer hair cell driven oscillatory fluid flow in the tunnel of corti. *Biophys. J.* 92:3284–3293.
78. Kinsler, L. E. 2000. Fundamentals of Acoustics. Wiley, New York.
79. Lee, H. Y., P. D. Raphael, …, J. S. Oghalai. 2016. Two-dimensional cochlear micromechanics measured in vivo demonstrate radial tuning within the mouse organ of corti. *J. Neurosci.* 36:8160–8173.
80. Johnson, S. L., M. Beurg, …, R. Fettiplace. 2011. Prestin-driven cochlear amplification is not limited by the outer hair cell membrane time constant. *Neuron.* 70:1143–1154.
81. Meaud, J., and K. Grosh. 2012. Response to a pure tone in a nonlinear mechanical-electrical-acoustical model of the cochlea. *Biophys. J.* 102:1237–1246.